




## Flow mode and global transport of liquid metal thermal convection in a cavity with $\Gamma = 1/3$

Xin-Yuan Chen (陈新元)  and Juan-Cheng Yang (阳倦成) <sup>\*</sup>

*State Key Laboratory for Strength and Vibration of Mechanical Structures, School of Aerospace,  
Xi'an Jiaotong University, Xi'an 710049, China*

Ming-Jiu Ni (倪明玖) <sup>†</sup>

*State Key Laboratory for Strength and Vibration of Mechanical Structures,  
School of Aerospace, Xi'an Jiaotong University, Xi'an 710049, China;  
School of Engineering Science, University of Chinese Academy of Sciences, Beijing 100049, China*



(Received 8 October 2023; accepted 9 January 2024; published 20 February 2024)

We report an experimental study of Rayleigh-Bénard convection of liquid metal thermal convection with a Prandtl number of  $Pr = 0.029$  in the cuboid cell of aspect ratios  $\Gamma = \text{width/height} = 1/3$ . By arranging 48 thermistors and 6 ultrasonic sensors in the sidewall of the cell, the flow mode and corresponding flow and heat transfer characteristics are obtained with Rayleigh number  $Ra$  varying from  $1.05 \times 10^6$  to  $4.01 \times 10^7$ . Three typical flow modes are defined from the results of temperature measurements, showing a double-roll mode (DRM) with two vertically stacked counterrotating rolls, a single-roll mode (SRM) that occupies the entire cell and a distorted single-roll mode existing in the transitions between DRM and SRM. Moreover, by gradually increasing the  $Ra$  one can observe the flow transition from DRM to SRM by the statistics of the lifetime for each flow mode. The complete Fourier analysis of temperature data shows that the origin of the flow modes can be attributed to the energy transformation between Fourier modes of different orders. When  $Ra \geq 1.19 \times 10^7$ , the first Fourier mode energy has accounted for more than 75% of the total energy which is evidence that the SRM is fully established. Furthermore, the measured temperature profiles along the central axis of the cell follow a linear law in the bulk, and the slopes obey power-law scaling with  $Ra$ . Regarding the standard deviation of temperature profiles along the central axis of the cell which bulge in the bulk forming the second peak outside the thermal boundary layers at small  $Ra$  due to the complex three-dimensional flow structures. Finally, the similar scaling laws of the global heat and momentum transfer of the liquid metal thermal convection in a slender cuboid cell are observed, showing  $Nu \sim Ra^{0.35}$  and  $Re \sim Ra^{0.36}$  for heat and momentum transfer, respectively.

DOI: [10.1103/PhysRevFluids.9.023503](https://doi.org/10.1103/PhysRevFluids.9.023503)

### I. INTRODUCTION

Liquid metal thermal convection is ubiquitous in nature and industrial applications, for example, convection in the Earth's outer core [1,2] and in the blanket of the nuclear fusion reactors [3]. A well-known paradigmatic system for studying thermal convection in the laboratory is Rayleigh-Bénard convection (RBC) which can be briefly described as the fluid layer being heated (cooled)

---

<sup>\*</sup> yangjc@xjtu.edu.cn

<sup>†</sup> mjni@ucas.ac.cn

by the lower (upper) plate. The fluid is driven by the buoyancy induced by the temperature gradient to form self-organization motion [4–6]. Three dimensionless parameters control such a convection system, namely, the Rayleigh number  $Ra = \alpha g \Delta T H^3 / \nu \kappa$  represents the ability of thermal driving, the Prandtl number  $Pr = \nu / \kappa$ , as well as the aspect ratio  $\Gamma = D/H$  denotes the effect of the spatial confinement. Here  $\alpha$ ,  $g$ ,  $\nu$ , and  $\kappa$  are the thermal expansion coefficient, the gravitational acceleration constant, the kinematic viscosity, and thermal diffusivity, respectively;  $\Delta T$  is the temperature difference between the two plates;  $D$  and  $H$  are the width and height of the cell. Moreover, there are two key system response parameters, namely, the Nusselt number  $Nu = qH/\lambda\Delta T$  quantifies the heat transport efficiency, where  $q$  is the power supplied to the cell which can be regarded as heat flux transported by the fluid, and  $\lambda$  is the thermal conductivity of the fluid, and the Reynolds number  $Re = vH/\nu$  identifies the momentum transport efficiency, where  $v$  is the velocity of the flow.

Due to the thermal boundary layer (BL) instability, a partial separation of the thermal BL occurs, forming the so-called plumes. The rising and falling motions of the plumes shear the surrounding flow field that initiates the large-scale flow (LSF) [6,7]. A typical feature of LSF is the so-called large-scale circulation (LSC), the product of fully developed LSF. Recently, researchers have devoted significant efforts to studying the structure of LSC and its dynamic characteristics. The main feature of the LSC is the single-roll structure (SRS), which occupies almost the entire convection cell. The LSC exhibits some intriguing flow dynamics like torsional and sloshing modes occasionally. The torsional mode refers to the case that the upper and lower parts of the LSC show periodic oscillation in opposite directions, while the sloshing mode of LSC shows time-periodical oscillation around the cell's central vertical axis [8–13]. However, due to the potential well of the cubic cell, the LSC convection plane is restricted to the diagonal with occasional diagonal-switching [14,15]. As reported by a recent numerical simulation [16], the LSC convection plane in a cubic cell may align along a pair of opposite side faces and the decoherent state without any well-defined LSC can also be found [16]. In addition, flow cessations occasionally occur, resulting in the LSC breakdown and reorganization with a different orientation [17–19]. Although numerical simulations can provide fruitful physical information with fine time-space resolution to elucidate convection phenomena. They require huge computing resources and are not suitable to obtain the phenomena for a long physical time for the thermal convection of low-Prandtl number fluids due to the extremely small Kolmogorov scale [20,21]. Therefore, employing experimental methods enables long-term measurements, allowing for the acquisition of ample statistical data and the observation of the evolution of flow modes over an extended period.

The aspect ratio  $\Gamma$  also plays an essential role in the flow structures. For the cells with  $\Gamma$  larger than 1, the flow pattern usually presents the form of multiple-roll arranged side by side [22,23]. Recently, combining the numerical simulation and experiments, a new flow structure called “jump-rope-vortex” was reported in  $\Gamma = 2$  and 5 [24,25]. The oscillations of the large-scale circulation in liquid metal convection are well studied from  $\Gamma = 1.4$  to 3 [26]. However, an elongated cell (i.e.,  $\Gamma < 1$ ) leads to the formation of a multiroll structure stacked along the height of the cell, e.g., double-roll structure (DRS) [8,9,27] or appear axisymmetric toroidal rings near the top and bottom plate [28]. The observed transition between a single-roll structure (SRS) and a multiroll structure can be attributed to the elliptical instability [29,30]. The current research on elongated cells with small  $\Gamma$  primarily focuses on those with  $\Gamma \leq 1/5$  [29,31,32], while limited attention has been given to the range  $1/5 \leq \Gamma \leq 1$ . In this particular range, where the LSF is influenced by geometric confinement, the transition between flow structures can be readily observed, an aspect that has not been thoroughly investigated. Additionally, flow structures and dynamics exhibit differences in elongated cubic or cuboid cells compared to cylindrical cells. Notably, sloshing and torsional modes are scarcely observed in cubic or cuboid cells due to their lack of perfect symmetry to cylindrical cells. Consequently, understanding how flow dynamic characteristics and other quantitative results in an elongated cuboid cell differ from those in previous studies poses an open question and serves as the main objective of our present study. To bridge the gap between  $1/5 \leq \Gamma \leq 1$  and explore flow characteristics in a cuboid cell, a convection cell with  $\Gamma = 1/3$  proves suitable for this investigation.

Moreover, regarding the low Prandtl number, the thermal diffusivity of liquid metal is much greater than the kinematic viscosity resulting in the change in the relative thickness of the thermal and viscous BL, i.e., the viscous BL is immersed in the thermal BL. Without the protection of the viscous BL, the LSF will act directly on the thermal BL contributing to more violent temperature fluctuations in the convection cell. Generally speaking, the temperature profile is consistent with the Prandtl-Blasius (PB) profile, i.e., the temperature tends to the average temperature in bulk, and inside the BL, it shows a linear distribution [33–36]. The corresponding temperature standard deviation profile has a peak near the edge of the thermal BL and then diminishes in the center of the cell. Whereas, these quantities are not well-studied in liquid metal thermal convection in the cuboid cell with small  $\Gamma$ .

The global transport of heat and momentum is critical in evaluating a convection system. One of the main issues in thermal convection is to find out the relationship between global transport and the three control parameters. Early studies on the heat transport of liquid metal thermal convection were carried out in the cell with large  $\Gamma$  [37,38]. For mercury with  $Pr \approx 0.025$  and the gallium-indium-tin (GaInSn) alloy with  $Pr \approx 0.029$  in the cells with  $\Gamma \geq 1$ , the measurement results followed a power law scale of  $Nu \sim Ra^{0.25}$  [2,38–41] which agreed well with the prediction of Grossmann-Lohse (GL) theory [42,43]. However, for the elongated cell with  $\Gamma < 1$ , the scaling exponents are larger than 0.25 [28,44–46], which may be attributed to those mentioned above complex three-dimensional flow structure. It is well known that the plumes transported by the LSC carry the heat, meanwhile, the structure of the LSC also influences transport efficiency in some way. For example, the Nusselt number difference between SRS and DRS is less than 0.5% for  $\Gamma = 1/3$  [9] and is up to 1.6% for  $\Gamma = 0.5$ , and  $Pr = 4.38$  [27]. The visualization of the flow field offers a crucial perspective on the flow structure and its dynamics. However, one major problem hampering the velocity measurement of liquid metal is its opaque property which increases the difficulty of velocity measurement. Utilizing numerical simulations enables the acquisition of a velocity field with higher precision. Furthermore, this approach facilitates the calculation of the corresponding Reynolds number [47–49]. For the experimental study, the lag time of the temperature correlation between two adjacent probes on the sidewall provides an indirect method of velocity measurement and also can provide the temperature information along the cell height [31]. In this study, the ultrasound Doppler velocimetry (UDV) [50] which provides a noninvasive way of velocity measurement and was successfully applied in liquid metal thermal convection experiments [26,51–53] is used to measure velocity for higher accuracy.

In this paper, we report experimental measurements of liquid metal GaInSn thermal convection in a cuboid cell with  $\Gamma = 1/3$  by the following structure. In Sec. II, we briefly introduce our experimental setup and methods used in this study. In Sec. III, the evolution of flow modes and their quantitative properties are presented. The temperature and its standard deviation profile are discussed in Sec. IV. Section V reviews the global transport of heat and momentum. In Sec. VI, the main findings are summarized.

## II. EXPERIMENTAL SETUP AND METHODS

Our experiments are performed in a cuboid cell with aspect ratio  $\Gamma = D/H \approx 1/3$  ( $H = 15.1$  cm,  $D = 5.0$  cm). The sidewall is made of polymethyl methacrylate (PMMA) with a thickness of 0.5 cm. Due to the low thermal conductivity of PMMA, the sidewall boundary condition can be considered adiabatic. The cell is sandwiched between two oxygen-free copper plates which are electroplated with nickel to prevent liquid metal from corroding the interfaces. The upper plate served as a cooling chamber that removes the heat from the surface via a thermostat (XIATECH C3150A) whose temperature stability can reach  $\pm 0.01$  °C. The water is circulated in the dual symmetrical channels on the back of the copper plate, so the temperature uniformity of the copper surface is maintained well. The lower plate is heated by resistance wire (OMEGA NI80) buried in the grooves on the back of the plate. A programmable DC power supply (GWINSTEK PSW 250-13.5) is used to provide constant voltage on the wire. The temperature constancy can be evaluated by the Biot

TABLE I. The physical properties of GaInSn at 35 °C [55,56].

Mass density (kg m <sup>-3</sup> )	$\rho = 6.34 \times 10^3$
Kinematic viscosity (m <sup>2</sup> s <sup>-1</sup> )	$\nu = 3.15 \times 10^{-7}$
Thermal conductivity (W m <sup>-1</sup> K <sup>-1</sup> )	$\lambda = 24.9$
Thermal diffusivity (m <sup>2</sup> s <sup>-1</sup> )	$\kappa = 1.08 \times 10^5$
Thermal expansion coefficient (K <sup>-1</sup> )	$\alpha = 1.24 \times 10^{-4}$

number defined as

$$\text{Bi} = \text{Nu} \left( \frac{\lambda}{\lambda_{\text{Cu}}} \right) \left( \frac{H_{\text{Cu}}}{H} \right), \quad (1)$$

where  $\lambda$  and  $\lambda_{\text{Cu}}$  are the thermal conductivity of the liquid metal and copper, respectively.  $H_{\text{Cu}}$  is the thickness of the lower plate with 2.1 cm. Therefore, the Bi number ranges between  $0.029 \leq \text{Bi} \leq 0.104$  which is far less than 1 indicating the boundary conditions are almost isothermal [53,54]. To minimize heat loss, we take the following steps. Firstly, the whole apparatus is enveloped with a 3-cm-thick layer of insulation foam and positioned on a heating basin covering the lower plate. This heating basin ensures uniform temperature, matching that of the lower plate, thereby hindering outward heat diffusion. Furthermore, an incubator is constructed to maintain the ambient temperature close to the mean temperature of the fluid. The selected working fluid is the eutectic alloy GaInSn, characterized by a melting point of 10.5°C. The physical properties of GaInSn at a temperature  $\bar{T} = 35^\circ\text{C}$  can be found in Refs. [55,56] and also listed in Table I.

The temperature measurements rely on the thermistors (OMEGA 44031), calibrated together inside a thermostat. The calibration temperature is from 10°C to 50°C, and the resistances are measured continuously for one hour at each temperature to obtain the corresponding average resistances. Based on the Steinhart-Hart equation, the corresponding temperatures can be calculated by the measured thermistor resistances. Fluctuations of recorded temperature in equilibrium had a standard deviation of 4–7 mK. Therefore, the temperatures measured by the thermistors are reliable. The temperature difference,  $\Delta T = T_b - T_t$ , is measured by the four thermistors in each plate. The four thermistor tips are only 2 mm away from the interface between copper and liquid metal, so that the upper and lower boundary temperatures can be accurately measured. Forty thermistors are mounted on the sidewalls to be distributed on five horizontal layers along the height,  $H/6$ ,  $2H/6$ ,  $3H/6$ ,  $4H/6$ , and  $5H/6$  as shown in Fig. 1(a). On each layer, eight thermistors are equally spaced in the azimuth and placed in the blind holes drilled from the outside into the sidewall. The end of these blind holes is 0.5 mm from the fluid-contact surface. To achieve better thermal contact, each blind hole is filled with thermally conductive silicone grease. All thermistors are connected to two multichannel multimeters (KEYSIGHT DAQ970A), and their resistances are acquired simultaneously at a sampling frequency of 0.6 Hz. Times are given in units of the free-fall time  $\tau_{\text{ff}} = \sqrt{H/g\alpha\Delta\bar{T}}$ . Each experimental test run is conducted 10 000 free-fall times to ensure the collection of ample statistical data.

We adopt the ultrasound Doppler velocimeter (UDV), which is based on the principle of Doppler frequency shift to measure the velocities of liquid metal flow. In the present experimental system, six UDV transducers with a diameter of 0.8 cm are mounted on the sidewall to obtain the velocities in two orthogonal directions, i.e.,  $v_x$  and  $v_y$ , respectively. Three UDV transducers with an emitting frequency of 8 MHz are arranged on the central axis of the same wall to measure the velocity in the  $x$  direction. Two are placed close to the upper and lower plates at a distance of 10 mm. The other is placed in the midheight of the sidewall. The other three transducers with an emitting frequency of 4 MHz are mounted on the adjacent wall to measure the velocity in the  $y$  direction, and they are on the same height plane as the three transducers in the  $x$  direction. The spatial and temporal resolution of velocity acquisition is estimated to be 0.4 mm and 0.8 s, respectively. By this arrangement, three crossing points with a two-dimensional velocity vector (i.e.,  $v_{\text{top}}$ ,  $v_{\text{mid}}$ , and

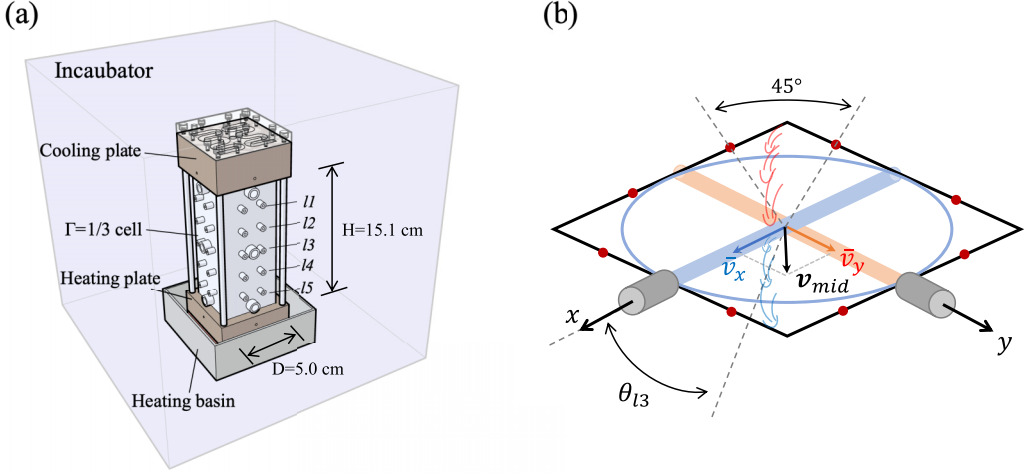


FIG. 1. (a) Sketch of the convection apparatus and constant temperature system. (b) UDV transducers and thermistors locations on  $l3$  layer. The UDV transducers measure the lateral  $v_x$  and  $v_y$  in the two orthogonal directions  $x$  and  $y$ , respectively. The mean velocity  $\bar{v}_x$  and  $\bar{v}_y$  are averaged from the 1 cm near the crossing point. These two values are used as components of the horizontal velocity vector, denoted as  $v_{mid}$  on this layer.  $\theta_{l3}$  is measured by the eight thermistors on the sidewall based on the relative position of the hot ascending and cold descending plumes and used as the orientation of the LSC.

$v_{bot}$ ) are established along the central axis of the cell, one of the three is shown in Fig. 1(b). The velocity profiles along each measurement line are sequentially acquired through multiplexing. To enhance echo reception, all transducers come into direct contact with the liquid metal GaInSn. We have incorporated a mixture of nickel and tungsten carbide powder with a diameter of approximately  $20 \mu\text{m}$  as tracers. In preliminary experiments, it was determined that the addition of a small quantity of powder particles does not impact the flow or its heat transport properties.

The multithermal-probe method which has been proven to be able to identify various flow modes successfully is adopted here to obtain the flow orientation and strength [9,39,57]. In thermal convection, when the hot plume rises or the cold plume descends, it will cause local high or low temperatures on the sidewall. Therefore, as long as the relative positions of high and low temperatures and the temperature difference between them are measured, the orientation and strength of the flow can be obtained. The function is fitted to each set of eight thermistors ( $i = 0, \dots, 7$ ) in one layer at each time step:

$$T(i, t)_k = T_0(t)_k + \delta_k(t) \cos(i\pi/4 - \theta_k(t)). \quad (2)$$

The time series of the flow strength  $\delta_k(t)$  and the flow orientation  $\theta_k(t)$  can be obtained. However, when the large-scale circulation breaks down, the above function can not fit the instantaneous effectively. Therefore, to further quantify the flow strength and orientation, the temperature profile was decomposed into four Fourier modes

$$T(i, t)_k = T_0(t)_k + \sum_{n=1}^4 \left[ a_{n,k}(t) \cos\left(\frac{n\pi}{4}i\right) + b_{n,k}(t) \sin\left(\frac{n\pi}{4}i\right) \right]. \quad (3)$$

Here,  $n = 1, \dots, 4$  are the  $n$ th Fourier mode and we obtain the time series of  $n$ th Fourier mode energy

$$E(t)_{n,k} = a_{n,k}^2(t) + b_{n,k}^2(t), \quad (4)$$

and the total energy of all modes

$$E(t)_{i,k} = \sum_{n=1}^4 E(t)_{n,k}. \quad (5)$$

Here, the index  $k$  stands for the height of the thermistor row labeled with “11,” “12,” “13,” “14,” and “15” from the top to the bottom of the cavity in the following sections. In the above functions,  $\bar{T}_k$  is the average temperature of the eight thermistors at each height [41,58].

### III. LARGE-SCALE FLOW DYNAMICS

#### A. Evolution of large-scale flow modes

We first discuss the evolution of LSC modes from single-roll mode (SRM) to double-roll mode (DRM) at the moderate Rayleigh number,  $Ra = 6.23 \times 10^6$ . To quantify the coherent of the LSC modes, we take the midheight layer 13 as the reference and the mutual orientation differences,  $\delta\theta_{k,13} = \theta_k - \theta_{13}$ , ( $k = 11, 12, 14, 15$ ), are defined and confined between  $[-180^\circ, 180^\circ]$  through simple mathematical processing.

The flow mode determination method is introduced in Refs. [9,27]. When the  $\delta\theta_{k,13} < 60^\circ$ , i.e., the up flow orientations measured at the layers  $k$  and 13 are mostly aligned vertically, it indicates that the flow between these two layers can be considered within the same roll. However, when the  $\delta\theta_{k,13} > 120^\circ$ , the up flow orientations of the two layers are no longer aligned vertically, suggesting the occurrence of a DRM. In addition, as the  $60^\circ \leq \delta\theta_{k,13} \leq 120^\circ$ , the transition mode (TM) occurs between the layers, which has not been discussed deeply in previous works. The entire evolution of flow modes is shown in Fig. 2. The time traces are divided into several parts to distinguish the flow modes clearly. For  $0 \leq t/\tau_{ff} \leq 30$ , the four orientation differences  $\delta\theta_{k,13}$  are all within  $[-60^\circ, 60^\circ]$  marked by the two horizontal solid lines in Fig. 2(a) illustrating that the flow establishes a well-defined coherent structure throughout the whole cell, as the sketch shown in Fig. 2(b). Note that when the flow is in the SRM, the LSC plane stays in the cell’s dialog plane which is the typical feature of turbulent Rayleigh-Bénard convection in a cell with square cross-section [15]. At  $t/\tau_{ff} \sim 30$ ,  $\delta\theta_{11,13}$  and  $\delta\theta_{12,13}$  start to increase with time and exceed the critical value, i.e.,  $\delta\theta_{k,13} = 60^\circ$  but not over  $\delta\theta_{k,13} = 120^\circ$ . Thus, the flow at 11, 12 has a relatively large deflection relative to 13. However,  $\delta\theta_{14,13}$  and  $\delta\theta_{15,13}$  still stay within  $[-60^\circ, 60^\circ]$  implying that the flow at 13, 14, and 15 is aligned vertically with each other. Therefore, the large-scale flow is somewhat distorted, as shown in Fig. 2(c). It can be found that the normalized flow strengths  $\delta_k/\Delta T$  of 11 and 12 begin to decrease as the degree of distortion increases. As the  $\delta\theta_{11,13}$  and  $\delta\theta_{12,13}$  continue to increase and exceed the critical line of DRM, i.e., the horizontal dashed lines in Fig. 2(a), while  $\delta\theta_{14,13}$  and  $\delta\theta_{15,13}$  are still close to zero, the large-scale flow is broken into two rolls which lasts about  $12\tau_{ff} \sim 60$  s. Figure 2(d) shows the typical feature of DRM with two vertically stacked counter-rotating rolls. The flow structure shown in Fig. 2(d) is asymmetrical due to the relatively weaker flow strength of 11 and 12 at DRM, thus, the upper roll is smaller than the lower one. As the flow strengths of 11 and 12 rise to the previous level gradually after the DRM, the large-scale flow is returned to the SRM. To summarize this part, our experimental study shows clearly that the large-scale flow consists of multiple flow modes with different characteristics and can be reconstructed from the sidewall temperature data.

#### B. Persistence of flow modes

To quantitatively characterize the persistence of each flow mode. We study the fraction of time  $w$  during which the system stayed in a given mode as a function of  $Ra$  is shown in Fig. 3(a), and the averaged lifetimes of the corresponding mode versus  $Ra$  are shown in Fig. 3(b). In Fig. 3(a), one can see that the fraction of time when the flow in the TM even occupies  $\sim 70\%$  for small  $Ra$ . Furthermore, the total fractions of time when the flow in the DRM and TM can reach almost 90%



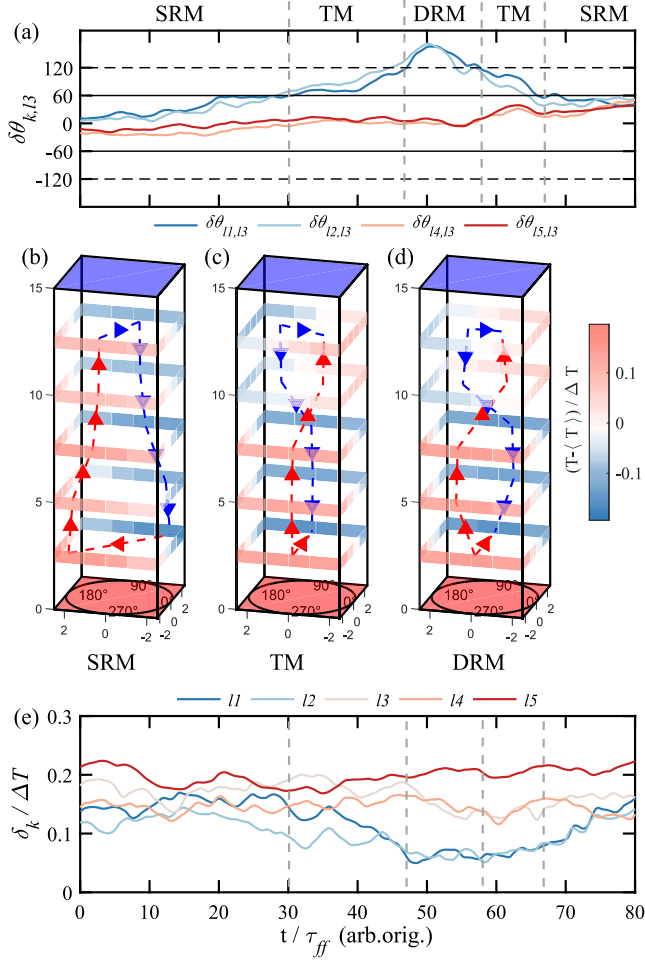


FIG. 2. Example of the evolution of flow modes from SRM to DRM at  $Ra = 6.23 \times 10^6$  and the free-fall time  $\tau_{ff} \approx 5.0s$ . Time trace of (a) the flow orientation differences between the other four horizontal layers and the midheight layer 13. The hottest (coldest) temperature points on the sidewall are connected with red (blue) lines at each layer to sketch the flow modes (b) SRM, (c) TM, and (d) DRM, respectively. The color bar represents the degree of the normalized temperature fluctuations. (e) Time trace of the normalized flow strength.

when  $Ra = 1.87 \times 10^6$ . However, with  $Ra$  increasing, the SRM time fraction increases, while the time fraction in the other two modes decreases. And at  $Ra = 8.23 \times 10^6$ , the fraction time of SRM and TM is close. When  $Ra > 1.19 \times 10^7$ , the fraction time of the SRM is larger than the other two modes and accounts for  $\sim 60\%$  of the total time. Thus, the so-obtained  $Ra = 1.19 \times 10^7$  can be regarded as a critical value,  $Ra_c$ , for the alternation of flow mode dominance as shown by the vertical dashed line in Fig. 3(a). As  $Ra > Ra_c$ , the time fraction of each mode changes slightly with the increase of  $Ra$ . Meanwhile, the fraction of time of the TM and DRM maintains a low level. Thus, the large-scale flow is dominated by the typical feature of turbulent RB convection, i.e., a single large-scale roll.

To better understand the dynamics of each mode, we further discuss the lifetime of modes. In Fig. 3(b), it can be seen that the average lifetimes of the TM and DRM vary from hundreds of seconds to tens of seconds with  $Ra$  increases. The tendencies of the TM and DRM lifetimes are

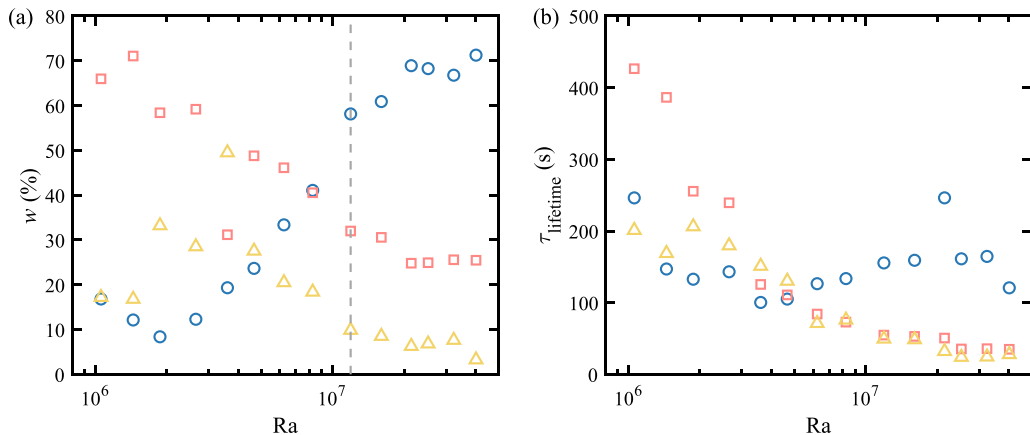


FIG. 3. (a) Percentage of the total run time during which the large-scale flow was in the SRM (circles), the TM (squares), and the DRM (triangles) as a function of Ra. The vertical dashed line indicates the critical Ra value,  $Ra_c = 1.19 \times 10^7$ . (b) Average lifetimes of the SRM, the TM, and the DRM.

similar to that of the fraction of time in Fig. 3(a), which also demonstrates the decline of the dominance of the TM and DRM. However, the average lifetime of SRM does not show a strong dependence on Ra and remains between 100 and 200 s. In previous studies on RB convection in water ( $Pr \sim 4.38$ ) [9,27], although the lifetimes of the double-roll mode decrease with increasing Ra, the decrease is not significant. Furthermore, the lifetimes are found to be smaller than those observed in our experiments with liquid metal ( $Pr \sim 0.029$ ). We speculate that in our experiment, due to the high thermal conductivity of liquid metal, the time fractions and average lifetimes of flow modes are sensitive to the change of Ra.

### C. Measurement of large-scale flow properties

A complete Fourier analysis of the temperature data can help us investigate the origin of the flow modes. An effective way to assess whether the SRM dominates or not is to calculate the parameter  $\overline{S}_k$  defined as

$$\overline{S}_k = \max \left[ \left( \frac{\langle E_{1,k} \rangle / \langle E_{t,k} \rangle - 1/(N_T/2)}{1 - 1/(N_T/2)} \right), 0 \right], \quad (6)$$

where  $N_T = 8$ . This parameter is first reported by Weiss *et al.* [59] and successfully quantifies the dominance or existence of large-scale flow in rotating RB convection and RB convection [41].  $\overline{S}_k = 1$  means that all of the Fourier energy is concentrated in the fundamental flow mode (i.e., SRM), while  $\overline{S}_k = 0$  represents the Fourier energy is distributed to the other flow modes. The value of  $\overline{S}_k$  is calculated and plotted against Ra in Fig. 4(a). With the increasing of Ra one can observe that the  $\overline{S}_k$  of each layer increases with different slopes. The increasing rates of  $\overline{S}_k$  for the layers near the upper and lower plates, i.e.,  $l1$  and  $l5$ , are the fastest, followed by  $l2$  and  $l4$  and the midlayer  $l3$  is the slowest. It can be explained that  $l1$  and  $l5$  are closer to the top and bottom thermal boundary layers where the plumes are emitted violently resulting stronger coherent flow structure, then the  $\overline{S}_k$  is larger even at small Ra. In addition, it can be observed that at the same Ra, the closer to the middle of the cell, the smaller the  $\overline{S}_k$  value, which means that the Fourier mode energy is more concentrated in the high-order Fourier modes rather than in the first mode in these layers. This is related to the occasional distortion or breakdown of the flow structure in the middle of the cell. According to Ref. [59], the closer  $\overline{S}_k$  is to 1, the more dominant the SRM is. In our experiment, when  $Ra \geq Ra_c$ , the  $\overline{S}_k$  of all five layers are close to 1, implying that the SRM prevailed, which is consistent with the results shown in Fig. 3(a).



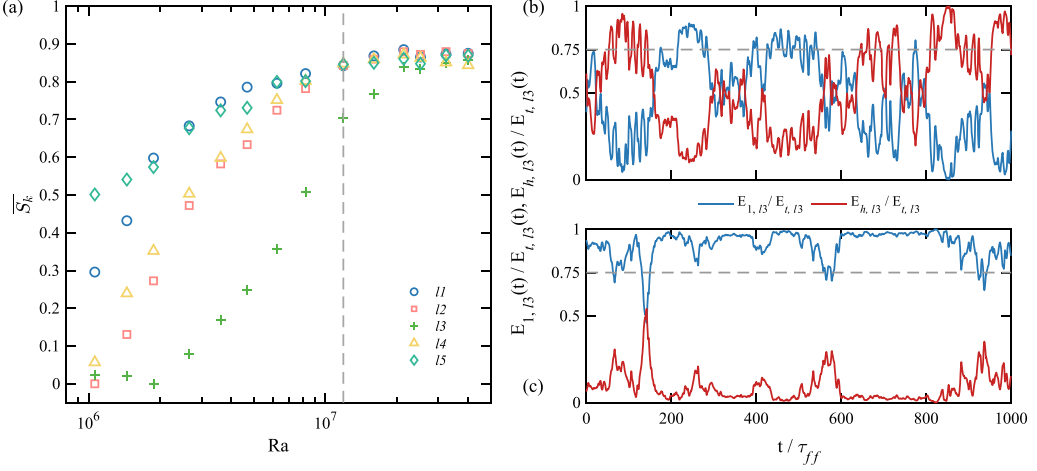


FIG. 4. (a) Parameter  $\overline{S}_k$  as a function of  $Ra$  for each horizontal layer. Panels (b) and (c) are the time series of the ratio of the first Fourier mode energy and the high-order Fourier mode energy to the total Fourier mode energy at  $Ra = 6.23 \times 10^6$  and  $Ra = 3.23 \times 10^7$ , respectively. The horizontal dashed lines indicate a value of 0.75.

The results obtained in different layers show similar dynamics, thus, we take the midlayer as an example to show the transformation between different Fourier modes. Figs. 4(b) and 4(c) shows the time series of  $E_{1,13}/E_{t,13}$  and  $E_{h,13}/E_{t,13}$ , here  $E_{1,13}$ ,  $E_{h,13}$ , and  $E_{t,13}$  means the first mode energy, the high-order mode energy, and the total Fourier energy of the 13 layer, respectively. According to Refs. [41,58], when  $E_{1,13}/E_{t,13}$  ( $E_{h,13}/E_{t,13}$ )  $\leq 0.75$  represented by the horizontal dashed lines in Figs. 4(b) and 4(c), the first mode (high-order modes) is considered as unstable. It can be clearly seen that in Fig. 4(b), the first mode and high-order modes dominate alternatively like the mode evolution shown in Fig. 2. However, in Fig. 4(c), when  $Ra = 3.23 \times 10^7$ ,  $E_{1,13}/E_{t,13}$  is almost larger than 0.75, suggesting that the first mode is dominance and the time fraction of the SRM is also reach almost 70%, correspondingly. In this part, we explain that the source of different flow modes is the energy transition between different Fourier modes. With the increase of the  $Ra$  number, the Fourier mode tends to be the first mode with a hallmark of a single-roll structure.

#### IV. TEMPERATURE PROFILE

The time-averaged temperature along the cell axis is shown in Fig. 5(a). It can be seen that the overall temperature profiles are similar for different  $Ra$ . In contrast to the typical temperature profile along the axis, where the temperature inside the boundary layer (BL) linearly varies with height, the temperature outside the BL exhibits minimal changes and remains close to the average temperature [60,61]. In an elongated cell, the temperature follows a linear law in the bulk flow which can be seen from Fig. 5(a) when  $40 \leq z \leq 75$  and in previous works [32,62]. In Fig. 5(b),  $T_c$  provides a better view of the temperature profile along the central axis across the entire cell, and the well-symmetrical profile is established. The linear temperature distribution area occupies almost the whole bulk. It can be explained that in a cell with a large aspect ratio, the fluid layer is fully mixed by the large-scale flow, making the bulk temperature more uniform and close to the average temperature of the fluid. However, for the cell with a small aspect ratio, the large-scale flow is closer to the sidewall, which makes the lower mixing degree of the bulk, resulting in an apparent linear temperature distribution as the process of pure heat conduction. The mean temperature of the five horizontal layers measured on the sidewall,  $T_s$ , close to the lower plate (upper plate) is higher (lower) than the  $T_c$  measured in the same height, indicating that the hotter (colder) flow is closer

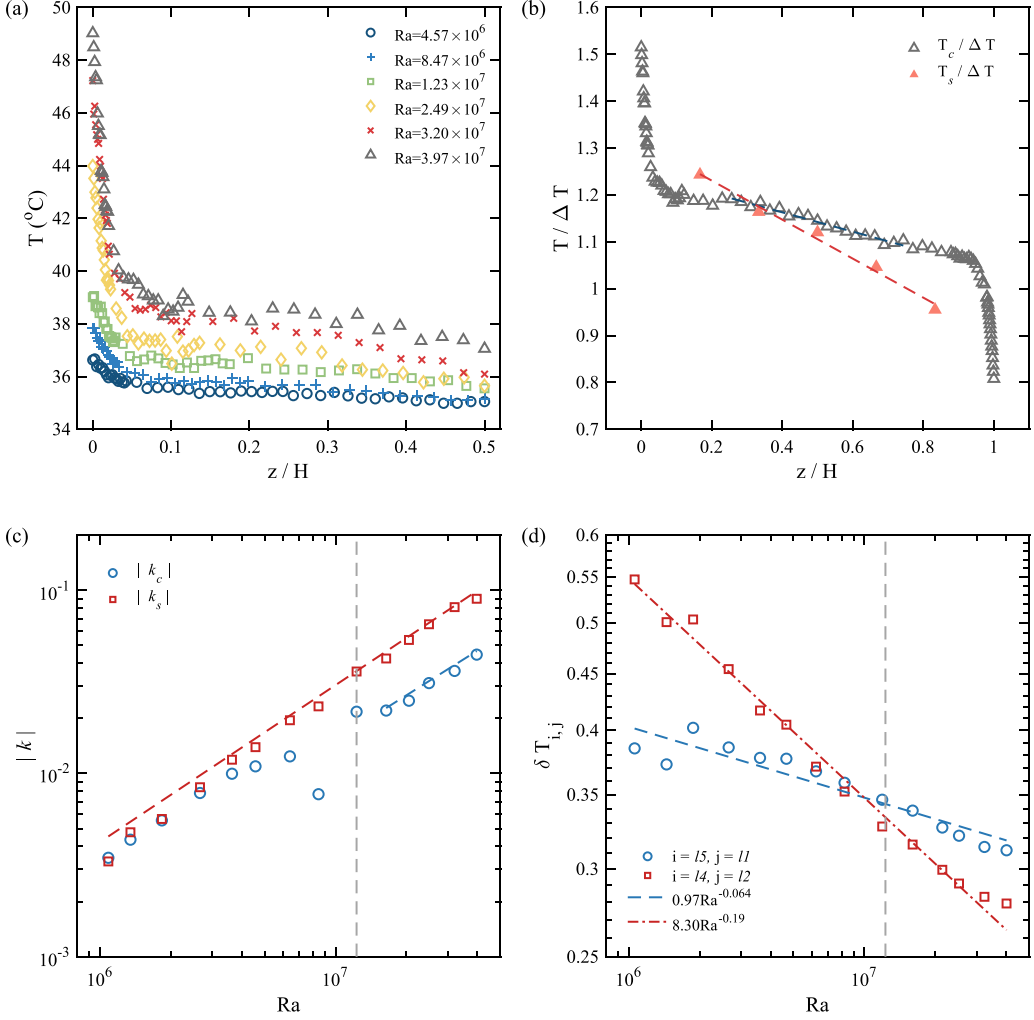


FIG. 5. (a) Time-averaged temperature along the central axis of the cell as a function of the height  $z$  at various  $Ra$ . (b) Example of the time-averaged temperature profile along the entire height of the cell (open symbols) and the mean temperature of the five horizontal layers (solid symbols) at  $Ra = 3.97 \times 10^7$ . The bulk flow temperature  $T_c$  and the sidewall temperature  $T_s$  are fitted by two linear functions, respectively, with respect to the height of the cell  $z$ . The slope of each linear fitting versus  $Ra$  is shown in panel (c). (d) Normalized vertical temperature gradients along the sidewall as a function of  $Ra$ .

to the sidewall rather than the center of the cell. To quantitatively characterize the attribution of the large-scale flow near the sidewall or the center, we carry out linear fitting for the temperature values at 19 points in the bulk and the mean temperature of the five horizontal layers, as shown by the dashed lines in Fig. 5(b) (the dashed lines are used for illustration purposes only). The slope of these two dashed lines ( $k_c$  and  $k_s$ , where subscript  $c$  denotes the temperature measured along the cell central axis and subscript  $s$  represents the mean temperature of the five layers on the sidewall) can be easily obtained from the fitting line and used to measure the magnitude of temperature changes along the height of the cell. The absolute values of  $k_c$  and  $k_s$  for the whole experimental range can be calculated and are plotted in Fig. 5(c). In general, for  $Ra \geq Ra_c$ ,  $|k_s|$  is more significant than  $|k_c|$ , but they are relatively close at a small  $Ra$  number. This is because the large-scale flow or SRM is not dominant at small  $Ra$ , and the occurrences of the TM and DRM also play a specific role in

mixing, which makes the sidewall temperature and the central temperature closer. This is also the reason why the temperature distribution in the bulk is less steep at a small Ra. Furthermore, when  $Ra \geq Ra_c$ , the exponent of power-law fitting for  $|k_c|$ , 0.81, is almost consistent with the result for  $|k_s|$ , 0.86, indicating that the temperature along the central axis and the sidewall increases by the same mechanism when Ra exceeds the critical  $Ra_c$ . It should be mentioned that the large drop of  $|k_c|$  around  $Ra_c$  is due to the temperature fluctuation during the flow state transition. However, the  $|k_s|$  does not show the drop as similar as the  $|k_c|$ , it can be attributed to the low-pass filtering effect of sidewall on the temperature fluctuations [63].

We calculate the gradient of temperature normalized by the  $\Delta T$  between the two layers symmetrical to each other relative to the midheight layer  $l3$  which is defined as

$$\delta T_{i,j} = |(\langle T_i \rangle - \langle T_j \rangle) / \Delta T|, \quad (7)$$

where  $i = l5$  ( $l4$ ) and  $j = l1$  ( $l2$ ). The results are shown in Fig. 5(d). It should be noted that the distance between  $l2$  and  $l4$  is half of  $l1$  and  $l5$ , so we multiply the corresponding temperature gradient by 2. In this way, the two temperature gradients can be comparable. In Fig. 5(d), the temperature gradients along the sidewall decrease with Ra and have a power-law with Ra, with exponents of  $-0.064$  and  $-0.19$ , respectively. Thus, it can be known that the sidewall's temperature gradient near the cell's midheight decays more rapidly with Ra increasing. When  $Ra \geq Ra_c$ , the temperature variation between  $l1$  and  $l5$  begins to be larger than that of  $l2$  and  $l4$ , suggesting that there is a significant temperature difference near the upper and lower plates. In contrast, the temperature difference near the midheight is smaller. The two temperature gradients cross near  $Ra_c$  corresponds to the aforementioned results that the SRM has been well-established as  $Ra > Ra_c$ . The smaller temperature variation near the midheight of the cell is also consistent with the essential characteristics of SRM [9].

The standard deviation of temperature over height along the central axis of the cell is another important parameter that reflects the fluctuation of the temperature, defined as  $\sigma_T = \sqrt{\langle (T(t) - \langle T(t) \rangle)^2 \rangle}$ .

In Fig. 6, we show the standard deviation profiles along the whole cell at various Ra. In turbulent thermal convection, the temperature fluctuation is most pronounced near the edges of the upper and lower thermal boundary layers, where the standard deviation reaches its maximum value. The distinct feature of turbulent thermal convection is the LSC occupies the entire cell. Most of the hot and cold plumes ascend or descend along the sidewall rather than through the bulk. Therefore, the temperature tends to be uniform in the bulk, so the standard deviation profile remains low and stable throughout the region. However, as we mentioned before, when  $Ra \leq Ra_c$ , the SRM is not dominant, and the flow is easily distorted or broken down in the bulk region, which results in large temperature fluctuations. Therefore, it can be seen from Figs. 6(a)–6(c) that the standard deviation profiles bulge in the bulk to form a second peak outside the BL, especially when the Ra is small, as shown in Fig. 6(a) that the standard deviations in the bulk are even larger than that near the BL edges. In Figs. 6(d)–6(f), as Ra increases, the SRM gradually dominates, the temperature fluctuations in the bulk flow begin to decrease, and the standard deviation profiles are consistent with fully developed turbulent thermal convection. The time series of the temperature fluctuation measure at the center of the cell also exhibits some kind of correlation with the Ra. In Figs. 7(a)–7(c), the frequency of fluctuations in the central temperature is small, and the fluctuations are not large and mainly limited in the range of  $[-3\sigma_T, 3\sigma_T]$  marked by the two vertical dashed lines in the corresponding probability density function (PDF) shown in Fig. 7(g). As the Ra increases, the fluctuation becomes significant with several spikes and sometimes exceeds  $3\sigma_T$ , which is caused by occasional plumes entering the bulk.

## V. GLOBAL TRANSPORT

The global transport properties in liquid metal convection are discussed here. Before the discussion, we make a brief summary of the heat transport results reported in previous studies in

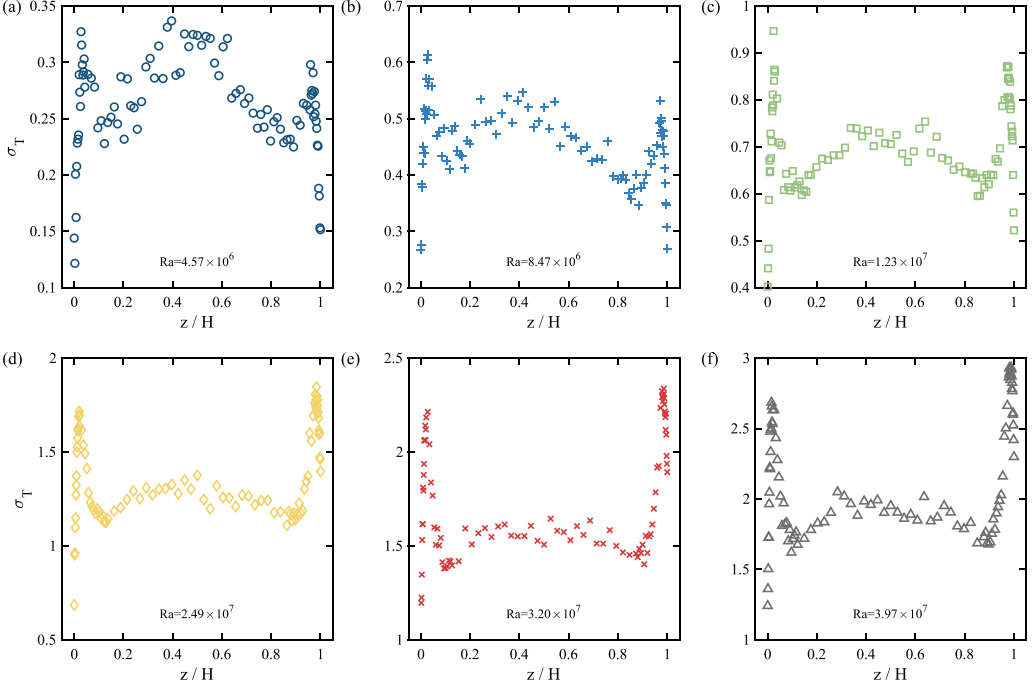


FIG. 6. The temperature standard deviations along the central axis of the cell as a function of the normalized height  $z/H$  at various  $Ra$ .

Table II. Regarding heat transport, in the RB convection system, a well-known system response parameter that measures the efficiency of heat transport is the Nusselt number,  $Nu$ . The data of our experiment are plotted versus  $Ra$  in Fig. 8(a), and we find  $Nu \sim Ra^{0.35}$ . The Grossmann-Lohse

TABLE II. Rayleigh number range, power-law for the Nusselt number, and cell geometries investigated in the previous studies on thermal convection with low-Prandtl number fluid.

Reference	$Ra$ range	$Nu$	Cell geometry
McDonald and Connoly (1960)	$4.8 \times 10^6 \leq Ra \leq 4.0 \times 10^7$	$Nu \sim Ra^{0.32}$	Cylinder ( $\Gamma \approx 1$ )
Rossby (1969)	$Ra \leq 8.7 \times 10^4$	$Nu \sim Ra^{0.257}$	Cylinder ( $\Gamma = 7.4, 22$ )
Kek and Müller (1993)	$Ra \leq 7.0 \times 10^3$	$Nu \sim Ra^{0.2}$	Cylinder ( $\Gamma = 11$ )
Takeshita <i>et al.</i> (1996)	$1 \times 10^6 \leq Ra \leq 1 \times 10^8$	$Nu \sim Ra^{2/7}$	Cylinder ( $\Gamma = 1$ )
Cioni <i>et al.</i> (1997)	$5 \times 10^6 \leq Ra \leq 5 \times 10^9$	$Nu \sim Ra^{0.26}$	Cylinder ( $\Gamma = 1$ )
Glazier <i>et al.</i> (1999)	$2 \times 10^5 \leq Ra \leq 8 \times 10^{10}$	$Nu \sim Ra^{0.285}$	Cylinder ( $\Gamma = 0.5, 1, 2$ )
Horanyi <i>et al.</i> (1999)	$1 \times 10^4 \leq Ra \leq 5 \times 10^6$	$Nu \sim Ra^{0.25}$	Cylinder ( $\Gamma = 4.5, 11, 20, 33$ )
Tsuji <i>et al.</i> (2005)	$1 \times 10^6 \leq Ra \leq 4 \times 10^8$	$Nu \sim Ra^{0.294}$	Cylinder ( $\Gamma = 0.5, 1, 2$ )
King <i>et al.</i> (2015)	$2 \times 10^6 \leq Ra \leq 2 \times 10^8$	$Nu \sim Ra^{0.249}$	Cylinder ( $\Gamma = 1$ )
Frick <i>et al.</i> (2015)	$2 \times 10^6 \leq Ra \leq 1 \times 10^7$	$Nu \sim Ra^{0.43}$	Cylinder ( $\Gamma = 1/5$ )
Mamykin <i>et al.</i> (2015)	$1 \times 10^6 \leq Ra \leq 6 \times 10^6$	$Nu \sim Ra^{0.77}$	Cylinder ( $\Gamma = 1/20$ )
Scheel and Schumacher (2017)	$3 \times 10^5 \leq Ra \leq 4 \times 10^8$	$Nu \sim Ra^{0.27}$	Cylinder ( $\Gamma = 1$ )
Zürner <i>et al.</i> (2019)	$1 \times 10^6 \leq Ra \leq 6 \times 10^7$	$Nu \sim Ra^{0.27}$	Cylinder ( $\Gamma = 1$ )
Ren <i>et al.</i> (2022)	$1 \times 10^6 \leq Ra \leq 1.3 \times 10^7$	$Nu \sim Ra^{0.25}$	Cylinder ( $\Gamma = 1$ )
Schindler <i>et al.</i> (2022)	$4 \times 10^5 \leq Ra \leq 5 \times 10^9$	$Nu \sim Ra^{0.28}$	Cylinder ( $\Gamma = 0.5, 1$ )

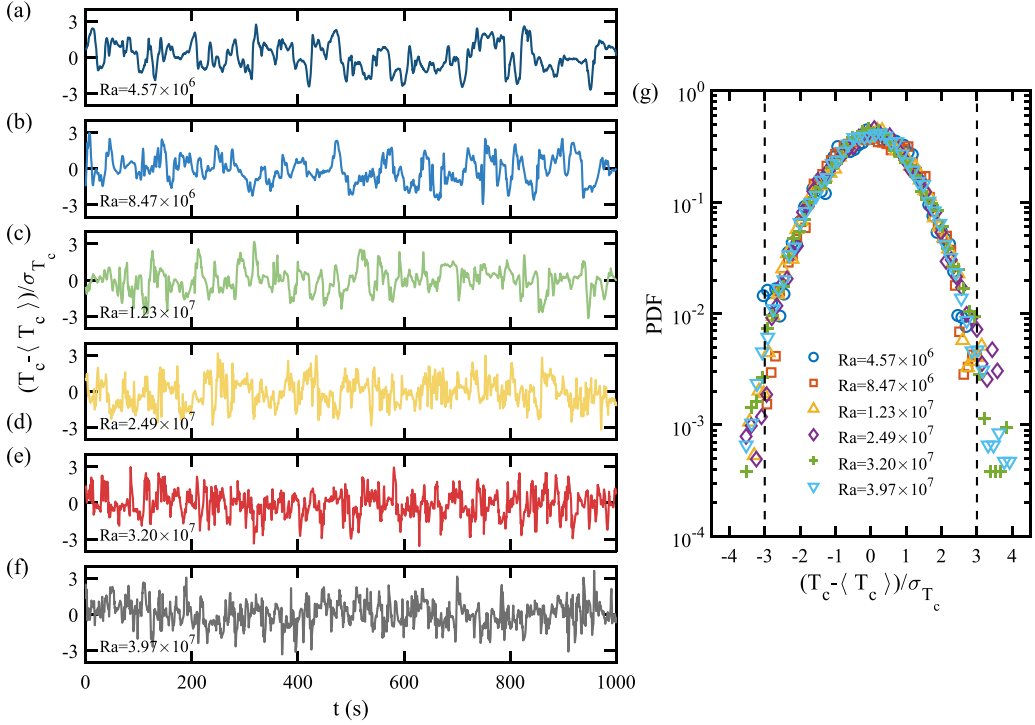


FIG. 7. (a)–(f) Time series of the temperature fluctuation at the cell center for different values of Ra. (g) PDF of the corresponding time series in panels (a)–(f).

(GL) model predicts  $Nu \sim Ra^{0.25}$  for  $Pr \ll 1$  [43] and it has been verified in many experiments, and numerical simulations with  $\Gamma = 1$ , e.g.,  $Nu \sim Ra^{0.26}$  for  $Pr = 0.025$  [39],  $Nu \sim Ra^{0.25}$  for  $Pr = 0.029$  [41], and  $Nu \sim Ra^{0.27}$  for  $Pr = 0.021$  [48]. For the larger aspect ratio, the GL model is also

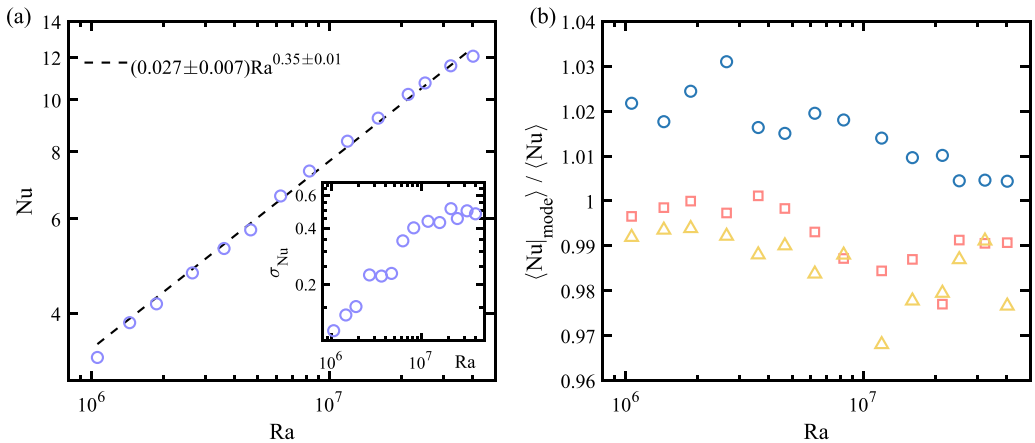


FIG. 8. (a) Nusselt number  $Nu$  as a function of the Rayleigh number  $Ra$  on logarithmic scales. The solid line is the best power-law fit for all the data. The inset plots the standard deviation of  $Nu$  vs  $Ra$ . (b) Normalized conditional average of  $Nu$ ,  $\langle Nu |_{mode} \rangle / \langle Nu \rangle$  for the SRM (circles), the TM (squares) and the DRM (triangles), respectively, where  $\langle Nu \rangle$  is  $Nu$  averaged over the entire run.

available, e.g., for  $\Gamma \sim 22$  and 7.4, they found  $\text{Nu} \sim \text{Ra}^{0.257}$  ( $\text{Pr} = 0.025$ ) [38], and for  $\Gamma \sim 11$ , they found  $\text{Nu} \sim \text{Ra}^{0.2}$  ( $\text{Pr} = 0.006$ ) [64]. However, in the cell with  $\Gamma < 1$ , also known as an elongated cell, the heat transport scaling exponents are larger than 0.25, i.e.,  $\text{Nu} \sim \text{Ra}^{0.294}$  for  $\Gamma \sim 1/2$  [28,44],  $\text{Nu} \sim \text{Ra}^{0.43}$  for  $\Gamma \sim 1/5$  [45] and  $\text{Nu} \sim \text{Ra}^{0.77}$  for  $\Gamma \sim 1/20$  [46]. Since the aspect ratio of our cell is  $1/5 \leq \Gamma = 1/3 \leq 1$ , our scaling exponent is also between 0.25 and 0.43 which can be explained by the effect of the increasing geometrical confinement [65]. It can be seen from Table II that the Ra range and the geometries of convection cells in the previous studies differ from those in our experiment. As indicated by the aforementioned results, the special geometry of our convection cell gives rise to complex three-dimensional flow structures. Additionally, the different Ra ranges also play an important role in the different heat transfer scaling laws. The inset in Fig. 8(a) plots the standard deviation of Nu,  $\sigma_{\text{Nu}} = \sqrt{\langle (\text{Nu} - \langle \text{Nu} \rangle)^2 \rangle}$ , over Ra which can be seen that the  $\sigma_{\text{Nu}}$  increases with Ra indicating that the fluctuation of Nu increases. However, when  $\text{Ra} \geq \text{Ra}_c$ , the  $\sigma_{\text{Nu}}$  seems to reach a plateau which is similar to the trend of  $\bar{S}_k$  in Fig. 4(a). From this, we know that the fluctuation of Nu increases when SRM gradually dominates, but when the flow is completely in the SRM, the fluctuation of Nu changes slightly as Ra increases.

Furthermore, to investigate the relationship between the Nusselt number and the internal flow modes, we calculate the normalized conditional average of Nu,  $\langle \text{Nu} |_{\text{mode}} \rangle / \langle \text{Nu} \rangle$ , for each mode separately, as shown in Fig. 8(b). The figure shows clearly that the Nu in the SRM is larger than that in the TM or DRM, which is evidence that the SRM is more efficient for heat transport than the TM and DRM. When the flow is in the DRM, a low-strength area is formed where the two rolls encounter, and the flow path becomes longer, which hinders the heat transported from the bottom to the top and increases the heat dissipation, so the Nusselt number of DRM is the smallest among the three modes [66]. However, the differences between the modes are small, quantitatively. The difference in Nu between SRM and DRM is up to 4%. The Nu differences induced by different flow modes are reported in some previous work, but they are smaller than our result. For example, the Nusselt number of the single-roll mode is larger than the double-roll mode by about 1.6% in Ref. [27], and only 0.5% in Ref. [9]. Noted that due to the small fraction of DRM ( $\sim 8\%$ ) when  $\text{Ra} \geq \text{Ra}_c$ , there are no sufficient statistics to calculate the corresponding conditional averages so that the data points are scattered slightly.

Another important global transport quantity is the Reynolds number, Re, characterizing momentum transport efficiency. As shown in Fig. 1(b), the velocity vector  $v$  is determined by the two orthogonal components  $\bar{v}_x$  and  $\bar{v}_y$ . The velocity  $\bar{v}_x$  and  $\bar{v}_y$  on each velocity measurement layer are obtained from the average of the data around the midpoint of the ultrasonic measurement line which is defined as

$$\bar{v}_i(t) = \langle v_i(j, t) \rangle_{-D/10 \leq j \leq D/10}, \quad (8)$$

with  $i = x, y$ . And the resulting velocity vector

$$v = (\bar{v}_x, \bar{v}_y). \quad (9)$$

The cell height  $H$  is chosen as the typical scale. According to different characteristic velocities, we can define three different Re: (1) root-mean-square value of LSC velocity defined as

$$v_{\text{LSC}} = \sqrt{\frac{\sum_{m=1}^M |v_{\text{top}} + v_{\text{bot}}|^2}{M}}, \quad (10)$$

(2) root-mean-square value of horizontal velocity near the two plates, i.e.,

$$v_{\text{top}} = \sqrt{\frac{\sum_{m=1}^M |v_{\text{top}}|^2}{M}} \quad (11)$$



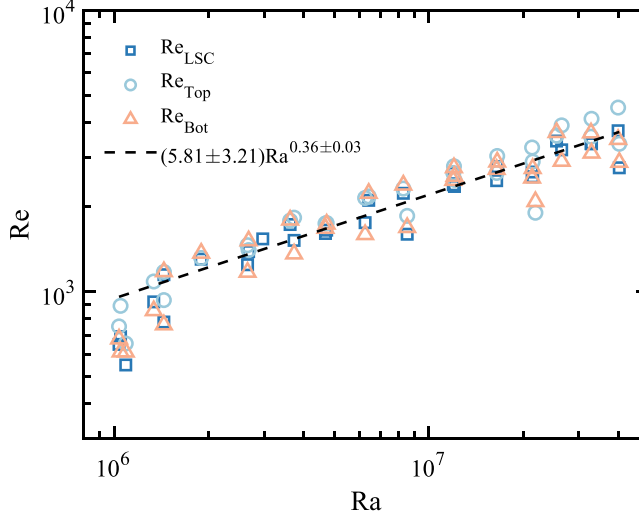


FIG. 9. Reynolds number  $Re$  as a function of the Rayleigh number  $Ra$  on logarithmic scales.

and

$$v_{\text{bot}} = \sqrt{\frac{\sum_{m=1}^M |v_{\text{bot}}|^2}{M}}, \quad (12)$$

where  $v_{\text{top}}$  and  $v_{\text{bot}}$  represent the velocities measured near the upper and lower plates, respectively, and  $M$  is the total data in the entire time series. Thus, we get three different  $Re$ , namely  $Re_{\text{LSC}}$ ,  $Re_{\text{top}}$  and  $Re_{\text{bot}}$ , the results can be seen in Fig. 9. The points in Fig. 9 exhibit slight scattering, attributed to flow fluctuations during UDV measurements. To mitigate uncertainties in the current measurements, velocity measurements were conducted at least twice for each  $Ra$ .

First, the momentum transport efficiency driven by LSC is characterized by the  $v_{\text{LSC}}$  and the resulting Reynolds number  $Re_{\text{LSC}} = v_{\text{LSC}}H/\nu$  is plotted in Fig. 9 with a power-law of  $Re_{\text{LSC}} = (6.06 \pm 4.8)Ra^{0.36 \pm 0.05}$ . At the highest  $Ra$ , the velocity of LSC is about 7.8 mm/s, thus the corresponding  $Re_{\text{LSC}}$  can reach  $3.67 \times 10^3$ . The scaling exponent 0.36 is close to that of  $Nu$ . The similarity of scaling exponents of heat transport and momentum transport in such a small aspect ratio cell agrees with the experimental results by Ref. [45]. However, the velocity in Ref. [45] is obtained from the correlation of temperatures measured by thermocouples equidistant along the height of the cell. In our experiment, we adopt the UDV technique to improve the measurement accuracy. Second, the horizontal velocities near the upper and lower plates are measured by the two UDV probes on each plane. It can be seen from Fig. 9 that the velocity of the upper and lower parts is relatively close, but by using the power-law fitting, the velocity of the scaling exponent of 0.39 for  $Re_{\text{top}}$ , and 0.35 for  $Re_{\text{bot}}$  are obtained indicating the velocity in the upper part increases a bit faster with  $Ra$ . To improve the fitting accuracy, we fit all the data together, and the fitting result is shown in Fig. 9.

To our knowledge, similar scaling behaviors of heat and momentum transport are uncommon in the cell with  $\Gamma \geq 1$  [25,48,51]. In the GL theory [42,43], for liquid metal GaInSn ( $Pr \ll 1$ ), the predicted power laws for  $Nu$  and  $Re$  are  $Nu \sim Ra^{0.25}$  and  $Re \sim Ra^{0.5}$ , respectively, which are not suitable for the transport efficiency measured in the small aspect ratio cell or such  $Ra$  range. A probable explanation is that the complex three-dimensional flow modes induced by the strong confinement of the geometry affect the transport efficiency, which requires more follow-up work to verify.

## VI. CONCLUSION

This paper presents a detailed experimental study of liquid metal thermal convection in a slender cuboid cell with  $\Gamma = 1/3$ . Liquid metal GaInSn was selected as the working fluid, the experiment covered a Rayleigh number range of  $1.05 \times 10^6$  to  $4.01 \times 10^7$  while the Prandtl number was fixed at 0.029.

Using the multithermal-probe method, how the flow modes change with time can be detected from the time series of flow orientation and strength. With the increase of  $Ra$ , the SRM gradually dominates while the probability of TM and DRM decreases. When  $Ra \geq 1.19 \times 10^7$ , the flow maintains SRM almost all the duration time. Therefore, in the present experimental conditions,  $Ra = 1.19 \times 10^7$  is considered the critical value  $Ra_c$  for the flow to transit to another states [41,58]. To find out the origin of flow modes, the temperature data was decomposed into four Fourier modes, and the energy of each Fourier mode was analyzed. As the  $Ra$  increases, the proportion of the first Fourier mode energy gradually increases. When  $Ra$  is greater than  $Ra_c$ , it can occupy more than 80% of the total energy. The first Fourier mode energy trend is similar to that of the SRM proportion. Meanwhile, the proportion of TM and DRM decreases with the decrease of the high-order mode energy, indicating that the transition of the flow mode is attributed to the energy distribution of the temperature at different Fourier orders.

The temperature measurement along the central axis also exhibits flow specificity in the small aspect ratio cells. In the bulk, the temperature follows a linear distribution due to a lack of full mixing. The time-averaged sidewall temperature also shows a linear profile along the height, with the same slope as the temperature of bulk flow at small  $Ra$ . When  $Ra$  is large enough, the slope of the linear profile versus  $Ra$  shows a power-law relationship, and the slope of the sidewall is much larger than that of the bulk flow. The profile of the temperature standard deviation measured along the central axis bulges in the bulk forming a second peak outside the thermal BLs. As  $Ra$  increases, the second peak vanishes and the typical temperature standard deviation profile of the turbulent thermal convection comes into being. Meanwhile, when  $Ra$  exceeds the critical value, the central temperature fluctuation becomes more violent as evidence that the flow enters another new state.

The heat and momentum transport are determined by the energy input from the lower plate and the velocity measured by UDV, respectively. An asymptotic power law described the Nusselt number as  $Nu \sim Ra^{0.35}$ . Compared with the TM and DRM, the  $Nu$  of the SRM can be enhanced by up to 4% since the DRM weakens the flow strength where the two stacked rolls rotating in opposite directions contact, which hinders the heat transfer. Another intriguing result is that the power law of Reynolds number, i.e.,  $Re \sim Ra^{0.36}$ , is similar to that of the Nusselt number, which is a peculiar phenomenon in the cells with a small aspect ratio.

This paper systematically explores the flow modes, temperature profiles, and global transport properties, which can inspire the study of thermal convection in liquid metals in small aspect ratio cells.

## ACKNOWLEDGMENTS

The authors gratefully acknowledge the support from National Key R&D Program of China (Grant No. 2022YFE03130000), National Natural Science Foundation (NSFC) (Grants No. 51927812, No. 52176089, and No. 52222607), and Young Talent Support Plan of Xi'an Jiaotong University.

[1] W. M. Elsasser, Hydromagnetic dynamo theory, *Rev. Mod. Phys.* **28**, 135 (1956).

[2] E. M. King and J. M. Aurnou, Turbulent convection in liquid metal with and without rotation, *Proc. Natl. Acad. Sci. USA* **110**, 6688 (2013).

- [3] J.-F. Salavy, L. Boccaccini, R. Lässer, R. Meyder, H. Neuberger, Y. Poitevin, G. Rampal, E. Rigal, M. Zmitko, and A. Aiello, Overview of the last progresses for the European Test Blanket Modules projects, *Fusion Eng. Des.* **82**, 2105 (2007).
- [4] G. Ahlers, S. Grossmann, and D. Lohse, Heat transfer and large scale dynamics in turbulent Rayleigh-Bénard convection, *Rev. Mod. Phys.* **81**, 503 (2009).
- [5] D. Lohse and K.-Q. Xia, Small-scale properties of turbulent Rayleigh-Bénard convection, *Annu. Rev. Fluid Mech.* **42**, 335 (2010).
- [6] K.-Q. Xia, Current trends and future directions in turbulent thermal convection, *Theor. Appl. Mech. Lett.* **3**, 052001 (2013).
- [7] H.-D. Xi, S. Lam, and K.-Q. Xia, From laminar plumes to organized flows: The onset of large-scale circulation in turbulent thermal convection, *J. Fluid Mech.* **503**, 47 (1999).
- [8] C. Sun, K.-Q. Xia, and P. Tong, Three-dimensional flow structures and dynamics of turbulent thermal convection in a cylindrical cell, *Phys. Rev. E* **72**, 026302 (2005).
- [9] H.-D. Xi and K.-Q. Xia, Flow mode transitions in turbulent thermal convection, *Phys. Fluids* **20**, 055104 (2008).
- [10] D. Funfschilling, E. Brown, and G. Ahlers, Torsional oscillations of the large-scale circulation in turbulent Rayleigh-Bénard convection, *J. Fluid Mech.* **607**, 119 (2008).
- [11] H.-D. Xi, S.-Q. Zhou, Q. Zhou, T.-S. Chan, and K.-Q. Xia, Origin of the temperature oscillation in turbulent thermal convection, *Phys. Rev. Lett.* **102**, 044503 (2009).
- [12] E. Brown and G. Ahlers, The origin of oscillations of the large-scale circulation of turbulent Rayleigh-Bénard convection, *J. Fluid Mech.* **638**, 383 (2009).
- [13] Q. Zhou, H.-D. Xi, S.-Q. Zhou, C. Sun, and K.-Q. Xia, Oscillations of the large-scale circulation in turbulent Rayleigh-Bénard convection: The sloshing mode and its relationship with the torsional mode, *J. Fluid Mech.* **630**, 367 (2009).
- [14] K. Bai, D. Ji, and E. Brown, Ability of a low-dimensional model to predict geometry-dependent dynamics of large-scale coherent structures in turbulence, *Phys. Rev. E* **93**, 023117 (2016).
- [15] D. Ji and E. Brown, Low-dimensional model of the large-scale circulation of turbulent Rayleigh-Bénard convection in a cubic container, *Phys. Rev. Fluids* **5**, 064606 (2020).
- [16] P. Maity, P. Koltai, and J. Schumacher, Large-scale flow in a cubic Rayleigh-Bénard cell: Long-term turbulence statistics and Markovianity of macrostate transitions, *Philos. Trans. R. Soc. London A* **380**, 20210042 (2022).
- [17] E. Brown, A. Nikolaenko, and G. Ahlers, Reorientation of the large-scale circulation in turbulent Rayleigh-Bénard convection, *Phys. Rev. Lett.* **95**, 084503 (2005).
- [18] E. Brown and G. Ahlers, Rotations and cessations of the large-scale circulation in turbulent Rayleigh-Bénard convection, *J. Fluid Mech.* **568**, 351 (2006).
- [19] H.-D. Xi and K.-Q. Xia, Cessations and reversals of the large-scale circulation in turbulent thermal convection, *Phys. Rev. E* **75**, 066307 (2007).
- [20] O. Shishkina, R. J. Stevens, S. Grossmann, and D. Lohse, Boundary layer structure in turbulent thermal convection and its consequences for the required numerical resolution, *New J. Phys.* **12**, 075022 (2010).
- [21] R. Ni, S.-D. Huang, and K.-Q. Xia, Local energy dissipation rate balances local heat flux in the center of turbulent thermal convection, *Phys. Rev. Lett.* **107**, 174503 (2011).
- [22] T. Yanagisawa, Y. Yamagishi, Y. Hamano, Y. Tasaka, M. Yoshida, K. Yano, and Y. Takeda, Structure of large-scale flows and their oscillation in the thermal convection of liquid gallium, *Phys. Rev. E* **82**, 016320 (2010).
- [23] T. Vogt, J.-C. Yang, F. Schindler, and S. Eckert, Free-fall velocities and heat transport enhancement in liquid metal magneto-convection, *J. Fluid Mech.* **915**, A68 (2021).
- [24] T. Vogt, S. Horn, A. M. Grannan, and J. M. Aurnou, Jump rope vortex in liquid metal convection, *Proc. Natl. Acad. Sci. USA* **115**, 12674 (2018).
- [25] M. Akashi, T. Yanagisawa, A. Sakuraba, F. Schindler, S. Horn, T. Vogt, and S. Eckert, Jump rope vortex flow in liquid metal Rayleigh-Bénard convection in a cuboid container of aspect ratio, *J. Fluid Mech.* **932**, A27 (2022).

- [26] J. S. Cheng, I. Mohammad, B. Wang, D. F. Keogh, J. M. Forer, and D. H. Kelley, Oscillations of the large-scale circulation in experimental liquid metal convection at aspect ratios 1.4–3, *J. Fluid Mech.* **949**, A42 (2022).
- [27] S. Weiss and G. Ahlers, Turbulent Rayleigh–Bénard convection in a cylindrical container with aspect ratio  $\gamma = 0.50$  and Prandtl number  $Pr = 4.38$ , *J. Fluid Mech.* **676**, 5 (2011).
- [28] Y. Tsuji, T. Mizuno, T. Mashiko, and M. Sano, Mean wind in convective turbulence of mercury, *Phys. Rev. Lett.* **94**, 034501 (2005).
- [29] L. Zvirner, A. Tilgner, and O. Shishkina, Elliptical instability and multiple-roll flow modes of the large-scale circulation in confined turbulent Rayleigh–Bénard convection, *Phys. Rev. Lett.* **125**, 054502 (2020).
- [30] X. He and P. Tong, Space-time correlations in turbulent Rayleigh–Bénard convection, *Acta Mech. Sin.* **30**, 457 (2014).
- [31] R. Khalilov, I. Kolesnichenko, A. Pavlinov, A. Mamykin, A. Shestakov, and P. Frick, Thermal convection of liquid sodium in inclined cylinders, *Phys. Rev. Fluids* **3**, 043503 (2018).
- [32] A. Pandey, D. Krasnov, J. Schumacher, R. Samtaney, and K. R. Sreenivasan, Similarities between characteristics of convective turbulence in confined and extended domains, *Physica D*, **442** 133537 (2022).
- [33] B. I. Shraiman and E. D. Siggia, Heat transport in high-Rayleigh-number convection, *Phys. Rev. A* **42**, 3650 (1990).
- [34] A. Belmonte, A. Tilgner, and A. Libchaber, Boundary layer length scales in thermal turbulence, *Phys. Rev. Lett.* **70**, 4067 (1993).
- [35] O. Shishkina, S. Horn, S. Wagner, and E. S. C. Ching, Thermal boundary layer equation for turbulent Rayleigh–Bénard convection, *Phys. Rev. Lett.* **114**, 114302 (2015).
- [36] H.-Y. Zou, W.-F. Zhou, X. Chen, Y. Bao, J. Chen, and Z.-S. She, Boundary layer structure in turbulent Rayleigh–Bénard convection in a slim box, *Acta Mech. Sin.* **35**, 713 (2019).
- [37] S. Globe and D. Dropkin, Natural-convection heat transfer in liquids confined by two horizontal plates and heated from below, *J. Heat Transfer* **81**, 24 (1959).
- [38] H. Rossby, A study of Bénard convection with and without rotation, *J. Fluid Mech.* **36**, 309 (1969).
- [39] S. Cioni, S. Ciliberto, and J. Sommeria, Strongly turbulent Rayleigh–Bénard convection in mercury: comparison with results at moderate Prandtl number, *J. Fluid Mech.* **335**, 111 (1997).
- [40] S. Horanyi, L. Krebs, and U. Müller, Turbulent Rayleigh–Bénard convection in low Prandtl–number fluids, *Int. J. Heat Mass Transf.* **42**, 3983 (1999).
- [41] L. Ren, X. Tao, L. Zhang, M.-J. Ni, K.-Q. Xia, and Y.-C. Xie, Flow states and heat transport in liquid metal convection, *J. Fluid Mech.* **951**, R1 (2022).
- [42] S. Grossmann and D. Lohse, Scaling in thermal convection: A unifying theory, *J. Fluid Mech.* **407**, 27 (2000).
- [43] R. J. Stevens, E. P. van der Poel, S. Grossmann, and D. Lohse, The unifying theory of scaling in thermal convection: The updated prefactors, *J. Fluid Mech.* **730**, 295 (2013).
- [44] T. Hayakawa and Y. Tsuji, Mean wind: Its velocity and temperature fluctuation in low-Prandtl-number thermal convection, *Physica D* **239**, 1353 (2010).
- [45] P. Frick, R. Khalilov, I. Kolesnichenko, A. Mamykin, V. Pakholkov, A. Pavlinov, and S. Rogozhkin, Turbulent convective heat transfer in a long cylinder with liquid sodium, *Europhys. Lett.* **109**, 14002 (2015).
- [46] A. Mamykin, P. Frick, R. Khalilov, I. Kolesnichenko, V. Pakholkov, S. Rogozhkin, and A. Vasiliev, Turbulent convective heat transfer in an inclined tube with liquid sodium, *Magnetohydrodynamics* **51**, 329 (2015).
- [47] J. D. Scheel and J. Schumacher, Global and local statistics in turbulent convection at low Prandtl numbers, *J. Fluid Mech.* **802**, 147 (2016).
- [48] J. D. Scheel and J. Schumacher, Predicting transition ranges to fully turbulent viscous boundary layers in low Prandtl number convection flows, *Phys. Rev. Fluids* **2**, 123501 (2017).
- [49] Z. L. Lim, K. L. Chong, G.-Y. Ding, and K.-Q. Xia, Quasistatic magnetoconvection: Heat transport enhancement and boundary layer crossing, *J. Fluid Mech.* **870**, 519 (2019).
- [50] Y. Takeda, Measurement of velocity profile of mercury flow by ultrasound Doppler shift method, *Nucl. Technol.* **79**, 120 (1987).

- [51] T. Zürner, F. Schindler, T. Vogt, S. Eckert, and J. Schumacher, Combined measurement of velocity and temperature in liquid metal convection, *J. Fluid Mech.* **876**, 1108 (2019).
- [52] J. C. Yang, T. Vogt, and S. Eckert, Transition from steady to oscillating convection rolls in Rayleigh–Bénard convection under the influence of a horizontal magnetic field, *Phys. Rev. Fluids* **6**, 023502 (2021).
- [53] F. Schindler, S. Eckert, T. Zürner, J. Schumacher, and T. Vogt, Collapse of coherent large scale flow in strongly turbulent liquid metal convection, *Phys. Rev. Lett.* **128**, 164501 (2022).
- [54] Y. Xu, S. Horn, and J. M. Aurnou, Thermoelectric precession in turbulent magnetoconvection, *J. Fluid Mech.* **930**, A8 (2022).
- [55] U. Müller and L. Bühler, *Magneto-fluid dynamics in Channels and Containers* (Springer Science & Business Media, Cham, 2001).
- [56] Y. Plevachuk, V. Sklyarchuk, S. Eckert, G. Gerbeth, and R. Novakovic, Thermophysical properties of the liquid Ga–In–Sn eutectic alloy, *J. Chem. Eng. Data* **59**, 757 (2014).
- [57] X. Zhu and Q. Zhou, Flow structures of turbulent Rayleigh–Bénard convection in annular cells with aspect ratio one and larger, *Acta Mech. Sin.* **37**, 1291 (2021).
- [58] P. Wei, The persistence of large-scale circulation in Rayleigh–Bénard convection, *J. Fluid Mech.* **924**, A28 (2021).
- [59] S. Weiss and G. Ahlers, The large-scale flow structure in turbulent rotating Rayleigh–Bénard convection, *J. Fluid Mech.* **688**, 461 (2011).
- [60] S.-L. Lui and K.-Q. Xia, Spatial structure of the thermal boundary layer in turbulent convection, *Phys. Rev. E* **57**, 5494 (1998).
- [61] N. Shi, M. S. Emran, and J. Schumacher, Boundary layer structure in turbulent Rayleigh–Bénard convection, *J. Fluid Mech.* **706**, 5 (2012).
- [62] A. Teimurazov and P. Frick, Thermal convection of liquid metal in a long inclined cylinder, *Phys. Rev. Fluids* **2**, 113501 (2017).
- [63] X. Chen, A. Xu, K.-Q. Xia, and H.-D. Xi, The effect of the cell tilting on the temperature oscillation in turbulent Rayleigh–Bénard convection, *Phys. Fluids* **35**, 085141 (2023).
- [64] V. Kek and U. Müller, Low Prandtl number convection in layers heated from below, *Int. J. Heat Mass Transf.* **36**, 2795 (1993).
- [65] L. Zvirner, R. Khalilov, I. Kolesnichenko, A. Mamykin, S. Mandrykin, A. Pavlinov, A. Shestakov, A. Teimurazov, P. Frick, and O. Shishkina, The influence of the cell inclination on the heat transport and large-scale circulation in liquid metal convection, *J. Fluid Mech.* **884**, A18 (2020).
- [66] R. Hartmann, K. L. Chong, R. J. Stevens, R. Verzicco, and D. Lohse, Heat transport enhancement in confined Rayleigh–Bénard convection feels the shape of the container (a), *Europhys. Lett.* **135**, 24004 (2021).